

Analytical solutions for the Extracellular-Membrane-Intracellular model

Carlos Ballesteros^a, Alexei Cheviakov^a, Raymond J. Spiteri^b

^a*Department of Mathematics and Statistics, University of Saskatchewan, 106 Wiggins Road, Saskatoon, S7N 5E6, Saskatchewan, Canada*

^b*Department of Computer Science, University of Saskatchewan, 110 Science Place, Saskatoon, S7N 5C9, Saskatchewan, Canada*

Abstract

The Extracellular-Membrane-Intracellular (EMI) model is a novel mathematical framework for cardiac electrophysiology simulations. The EMI model provides a more detailed description of the heart's electrical activity compared to traditional monodomain and bidomain models, potentially making it better-suited for understanding the electrical dynamics of the heart under pathological conditions. In this paper, we derive and verify several analytical solutions for the EMI model. Specifically, we obtain a family of solutions for a single two-dimensional cell in polar coordinates and for a pair of coupled three-dimensional cells in spherical coordinates. We also introduce a manufactured solution for N three-dimensional cells in Cartesian coordinates. To verify the analytical solutions, we conduct numerical experiments using the mortar finite element method combined with operator splitting. The results demonstrate that the analytical solutions are effective for verifying the accuracy of numerical simulations of the EMI model.

Keywords: Extracellular-Membrane-Intracellular model, Manufactured solution, Cardiac electrophysiology, Operator-splitting method, Mortar finite element method

1. Introduction

Mathematical models of cardiac electrophysiology are highly useful in understanding the propagation of electrical signals in the heart tissue. These models are used to study the effects of various physiological and pathological conditions, such as cardiac arrhythmias, on the electrical activity of the heart

and to develop new therapeutic strategies for their treatment. The most popular cardiac models are the monodomain and bidomain, which work well to simulate healthy tissue. However, these models have some limitations when it comes to simulating an unhealthy heart. To overcome these limitations, a new model called the extracellular-membrane-intracellular (EMI) model was developed [1]. This model considers the tissue as a collection of individual cells connected to each other, which is more realistic than the monodomain and bidomain models, where the tissue is considered as a single homogenized physical region.

Simulating heart tissue at the cellular level using the EMI model is computationally intensive due to the complexity and scale of the problem. This challenge has driven the development or implementation of various numerical methods, especially spatial discretization methods, such as the boundary element method [2], cut finite element method [3], mortar finite element method, and $H(\text{div})$ finite element method [1]. These implementations have, in turn, motivated the search for analytical solutions to validate the accuracy and performance of the numerical methods. To this end, researchers often opt for the application of manufactured solutions to simulate a single cell [1, 3, 4, 5], which provides a useful tool for convergence analysis. However, these solutions may not fully capture realistic scenarios.

In this work, we provide a detailed derivation of a family of analytical solutions for the EMI model that is more general and realistic than previous analytical solutions for one and two cells. We also introduce a manufactured solution for N three-dimensional cells. We numerically implement the EMI model using operator splitting in conjunction with the mortar finite element method to simulate simple examples from our solution family for one and two cells, as well as our manufactured solution, in order to verify the utility of the analytical solutions for benchmarking.

The paper is organized as follows. In Section 2, we provide a detailed description of the EMI model. In Section 3, we derive the family of analytical solutions. In Section 4, we describe the numerical implementation of the EMI model, and in Section 5, we present the numerical results for some simple solutions. Finally, in Section 6, we summarize our conclusions and outline directions for future work.

2. The Extracellular-Membrane-Intracellular model

The Extracellular-Membrane-Intracellular (EMI) model, also known as the cell-by-cell model [4, 2] was formally introduced by Tveito et al. [1] in 2017. Nonetheless, the model had been the subject of study for many years prior to that. [6, 7, 8]. The model is based on three physical spaces: the *intracellular* space, the intracellular-extracellular *membrane* (or cell membrane) space, and the *extracellular* space. The tissue is represented as a collection of cells spread across the extracellular space that communicate with one another via their membranes.

2.1. Governing equations

The complete mathematical description of the EMI model [1, 9] is presented as follows. Let Ω_e be a bounded domain representing the extracellular space, in which N cells are embedded, with its boundary denoted by $\partial\Omega_e$. For each cell k , the intracellular space is represented by the domain $\Omega_i^{(k)}$ with its boundary $\partial\Omega_i^{(k)}$. The intersection between the boundary of cell k and the boundary of the extracellular domain represents the membrane of the cell, denoted by $\Gamma_i^{(k)} := \partial\Omega_i^{(k)} \cap \partial\Omega_e$, while the intersection between the boundaries of two different cells k and ℓ , $\Gamma^{(k,\ell)} := \partial\Omega_i^{(k)} \cap \partial\Omega_i^{(\ell)}$, represents a gap junction. The outer boundary of the extracellular space is denoted by Γ_e . Figure 1 shows a two-dimensional configuration with four cells and the associated domains to illustrate the domains of the EMI model.

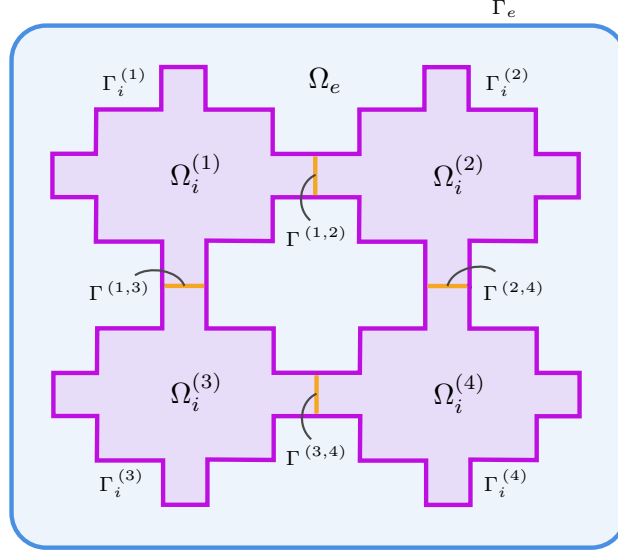


Figure 1: Configuration of a two-dimensional domain with four cells (purple) surrounded by extracellular space (blue) with gap junctions (orange) [1].

The intracellular potential $\Omega_i^{(k)}$ in the intracellular space of cell k is denoted by $u_i^{(k)}$, and the extracellular potential in the extracellular space Ω_e is denoted by u_e . The transmembrane potential of a cell k is divided into two parts, the transmembrane potential across the membrane, $v^{(k)}$, which is defined as

$$v^{(k)} = u_i^{(k)} - u_e, \quad \text{on } \Gamma_i^{(k)}, \quad (1)$$

and the transmembrane potential across the gap junctions $w^{(k,\ell)}$, which for an adjacent cell ℓ , is defined as

$$w^{(k,\ell)} = u_i^{(k)} - u_i^{(\ell)} \quad \text{on } \Gamma^{(k,\ell)}. \quad (2)$$

In each intracellular space $\Omega_i^{(k)}$ and the extracellular domain Ω_e , the intracellular and extracellular potentials satisfy

$$\nabla \cdot (\sigma_i \nabla u_i^{(k)}) = 0, \quad \text{in } \Omega_i^{(k)}, \quad (3a)$$

$$\nabla \cdot (\sigma_e \nabla u_e) = 0, \quad \text{in } \Omega_e, \quad (3b)$$

where the parameters σ_i and σ_e represent the conductivities of the intracellular and extracellular spaces, respectively, where for simplicity we assume σ_i is not cell-dependent. Furthermore, on each membrane $\Gamma_i^{(k)}$ and gap junction $\Gamma^{(k,\ell)}$, the transmembrane potentials $v^{(k)}$ and $w^{(k,\ell)}$ satisfy

$$C_m^{(k)} \frac{\partial v^{(k)}}{\partial t} = I_m^{(k)} - I_{\text{ion}}^{(k)}, \quad \text{on } \Gamma_i^{(k)}, \quad (4a)$$

$$I_m^{(k)} = (\sigma_e \nabla u_e) \cdot \hat{\mathbf{n}}_e = -(\sigma_i \nabla u_i^{(k)}) \cdot \hat{\mathbf{n}}_i^{(k)}, \quad \text{on } \Gamma_i^{(k)}, \quad (4b)$$

$$C_m^{(k,\ell)} \frac{\partial w^{(k,\ell)}}{\partial t} = I_m^{(k,\ell)} - I_{\text{gap}}^{(k,\ell)}, \quad \text{on } \Gamma^{(k,\ell)}, \quad (4c)$$

$$I_m^{(k,\ell)} = (\sigma_i \nabla u_i^{(k)}) \cdot \hat{\mathbf{n}}_i^{(k)} = -(\sigma_i \nabla u_i^{(\ell)}) \cdot \hat{\mathbf{n}}_i^{(\ell)}, \quad \text{on } \Gamma^{(k,\ell)}, \quad (4d)$$

where the parameter $C_m^{(k)}$ is the capacitance of the membrane $\Gamma_i^{(k)}$ per unit area, the ion currents $I_m^{(k)}$ and $I_{\text{ion}}^{(k)}$ are currents across the membrane $\Gamma_i^{(k)}$, and $\hat{\mathbf{n}}_i^{(k)}$ is the outward unit normal vector to $\partial\Omega_i^{(k)}$. The parameter $C_m^{(k,\ell)}$ is the capacitance of the gap junction $\Gamma^{(k,\ell)}$, $I_m^{(k,\ell)}$ is the ion current across the gap junction $\Gamma^{(k,\ell)}$, and $I_{\text{gap}}^{(k,\ell)}$ is the ion current due to the transmembrane potential $w^{(k,\ell)}$ at the gap junction. We note that at the gap junction $\Gamma^{(k,\ell)}$, the normal vectors $\hat{\mathbf{n}}_i^{(k)}$ from $\partial\Omega_i^{(k)}$ and $\hat{\mathbf{n}}_i^{(\ell)}$ from $\partial\Omega_i^{(\ell)}$ satisfy $\hat{\mathbf{n}}_i^{(k)} = -\hat{\mathbf{n}}_i^{(\ell)}$.

Let $t_0, t_f > 0$ be such that $t_0 < t_f$. The extracellular potential u_e is subject to either a Dirichlet boundary condition on $\Gamma_e \times [t_0, t_f]$,

$$u_e = u_{\text{app}}, \quad (5)$$

or a Neumann boundary condition

$$(\sigma_e \nabla u_e) \cdot \hat{\mathbf{n}}_e = I_{\text{app}}. \quad (6)$$

A cell model is added to the system to couple the transmembrane potentials $v^{(k)}$ and $w^{(k,\ell)}$ with the ion currents $I_{\text{ion}}^{(k)}$ and $I_{\text{gap}}^{(k,\ell)}$. Cell models fall into two categories: active and passive. An active cell model is usually nonlinear and includes multiple state variables (see, e.g., [10, 11, 12]). In contrast, a passive cell model is generally simpler, with the ion currents $I_{\text{ion}}^{(k)}$ and $I_{\text{gap}}^{(k,\ell)}$ assumed to depend linearly on the transmembrane potentials $v^{(k)}$ and $w^{(k,\ell)}$, respectively. For a passive cell model, these ion currents are represented as

$$I_{\text{ion}}^{(k)}(v^{(k)}) = \frac{1}{R_m^{(k)}} (v^{(k)} - v_{\text{rest}}), \quad (7)$$

$$I_{\text{gap}}^{(k,\ell)}(w^{(k,\ell)}) = \frac{1}{R_m^{(k,\ell)}} (w^{(k,\ell)} - w_{\text{rest}}). \quad (8)$$

In case an active cell model is used, the following equation is added to the system of equations describing the dynamics of the potentials:

$$\frac{\partial \mathbf{s}^{(k)}}{\partial t} = \mathbf{f}^{(k)}(t, \mathbf{s}^{(k)}, v^{(k)}), \quad \text{on } \Gamma_i^{(k)}, \quad (9)$$

where the vector field $\mathbf{s}^{(k)}$ describes the cellular state at the time $t \in [t_0, t_f]$, and the nonlinear vector field $\mathbf{f}^{(k)}$ represents the dynamics of the cell model. We note that when the passive cell model is implemented, the EMI model given by the equations (1), (2), (3), (4), (7), (8) subject to (5) or (6) is a linear system of partial differential equations.

3. Analytical solutions

In this section, analytical solutions are sought for some specific examples and cases of the EMI model using passive cell models. Although these solutions may not make physical sense, they provide a reference point for the validation of numerical methods implemented to solve real-world problems.

3.1. Single cell

Consider a two-dimensional single cell with a circular membrane surrounded by an outer circular layer representing the extracellular space, as shown in Figure 2. In this setup, no gap junctions are present.

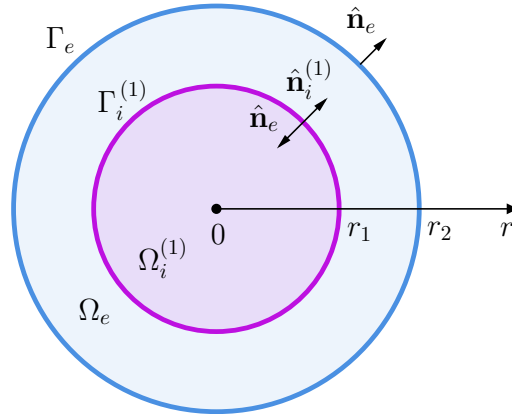


Figure 2: Domain representation for a single circular cell (purple) surrounded by a circular layer as extracellular space (blue).

Assuming that the transmembrane potential at the cell membrane is set to $v^{(1)} = v_0$ at $t = 0$, we are interested in finding an analytical solution to the following system of partial differential equations,

$$\nabla \cdot (\sigma_i \nabla u_i^{(1)}) = 0, \quad \text{in } \Omega_i^{(1)}, \quad (10a)$$

$$\nabla \cdot (\sigma_e \nabla u_e) = 0, \quad \text{in } \Omega_e, \quad (10b)$$

$$u_e = u_{\text{app}}, \quad \text{on } \Gamma_e. \quad (10c)$$

$$I_m^{(1)} = (\sigma_e \nabla u_e) \cdot \hat{\mathbf{n}}_e = -(\sigma_i \nabla u_i^{(1)}) \cdot \hat{\mathbf{n}}_i^{(1)}, \quad \text{on } \Gamma_i^{(1)}, \quad (10d)$$

$$v^{(1)} = u_i^{(1)} - u_e, \quad \text{on } \Gamma_i^{(1)}, \quad (10e)$$

$$C_m^{(1)} \frac{\partial v^{(1)}}{\partial t} = I_m^{(1)} - \frac{1}{R_m^{(1)}} (v^{(1)} - v_{\text{rest}}), \quad \text{on } \Gamma_i^{(1)}, \quad (10f)$$

$$v^{(1)}|_{t=0} = v_0, \quad \text{on } \Gamma_i^{(1)}. \quad (10g)$$

Using polar coordinates with the origin at the center of the cell and assuming radial symmetry, the potentials $u_i^{(1)}$ and u_e depend solely on the radial coordinate r . Solving the equations (10a) and (10b), the intracellular and extracellular potentials are given by

$$u_e = A_1 \int \frac{1}{\xi \sigma_e} d\xi + A_2, \quad (11a)$$

$$u_i^{(1)} = B_1 \int \frac{1}{\xi \sigma_i} d\xi + B_2, \quad (11b)$$

where A_1 , A_2 , B_1 and B_2 are the integration constants, which are generally arbitrary functions of time.

If we now consider the intracellular and extracellular conductivities to be equal, i.e.,

$$\sigma_e = \sigma_i, \quad (11c)$$

we can find a condition for A_1 and B_1 using equation (10d):

$$(\sigma_e \nabla u_e) \cdot \hat{\mathbf{n}}_e = -(\sigma_i \nabla u_i^{(1)}) \cdot \hat{\mathbf{n}}_i^{(1)} \implies B_1 = A_1 := A, \quad (11d)$$

and, consequently, the transmembrane current and potential take the forms

$$I_m^{(1)} = (\sigma_e \nabla u_e) \cdot \hat{\mathbf{n}}_e = -\frac{A}{r_1}, \quad (11e)$$

$$v^{(1)} = u_i^{(1)} - u_e = B_2 - A_2, \quad (11f)$$

respectively.

Now that $I_m^{(1)}$ is known, we can proceed to find the transmembrane potential $v^{(1)}$ by solving the initial value problem constructed with equations (10f) and (10g). The general solution to this system is given by

$$v^{(1)} = e^{-\frac{t}{C_m^{(1)}R_m^{(1)}}} \left(v_0 + \int_0^t \frac{e^{\frac{\tau}{C_m^{(1)}R_m^{(1)}}}}{C_m^{(1)}} \left(\frac{v_{\text{rest}}}{R_m^{(1)}} - \frac{A}{r_1} \right) d\tau \right). \quad (11g)$$

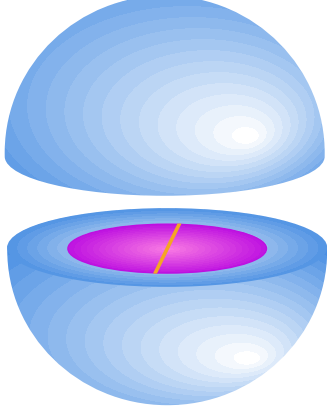
Finally, we can find a solution as long as the boundary condition is satisfied; i.e.,

$$u_e|_{r=r_2} = u_{\text{app}}. \quad (11h)$$

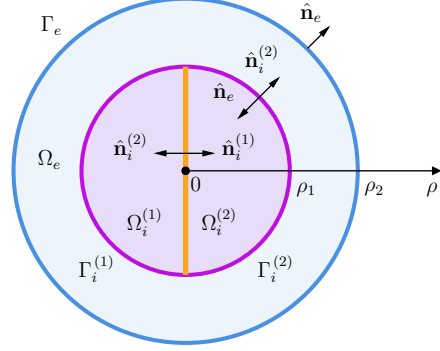
In summary, we have a family of solutions where $\sigma_e = \sigma_i$ (which can be the case for liposomes) and A and A_2 or B_2 are free to be chosen. The solutions presented here can be readily extended to a three-dimensional space, with a spherical cell and surrounding shell representing the extracellular space, under the assumption of radial symmetry.

3.2. Two coupled semi-spherical cells

Consider two semi-spherical cells connected along their circular bases and surrounded by a spherical shell of extracellular space as shown in Figure 3. We assume that the transmembrane potentials at the cell membranes are initially set to $v^{(k)} = v_k$ at $t = 0$ for $k = 1, 2$. Moreover, the transmembrane potential on the gap junction is initially set to $w^{(1,2)} = w_0$ at $t = 0$. Our objective now is to find a solution to the following linear system of partial



(a) Three-dimensional representation of two coupled semi-spherical cells.



(b) Two-dimensional cross-section of two semi-spherical cells.

Figure 3: Domain representation of two coupled semi-spherical cells (purple) connected by a gap junction (orange) and surrounded by a spherical shell-shaped extracellular space (blue).

differential equations:

$$\nabla \cdot (\sigma_i \nabla u_i^{(k)}) = 0, \quad \text{in } \Omega_i^{(k)}, \quad (12a)$$

$$\nabla \cdot (\sigma_e \nabla u_e) = 0, \quad \text{in } \Omega_e, \quad (12b)$$

$$u_e = u_{\text{app}}, \quad \text{on } \Gamma_e. \quad (12c)$$

$$I_m^{(k)} = (\sigma_e \nabla u_e) \cdot \hat{\mathbf{n}}_e = -(\sigma_i \nabla u_i^{(k)}) \cdot \hat{\mathbf{n}}_i^{(k)}, \quad \text{on } \Gamma_i^{(k)}, \quad (12d)$$

$$v^{(k)} = u_i^{(k)} - u_e, \quad \text{on } \Gamma_i^{(k)}, \quad (12e)$$

$$C_m^{(k)} \frac{\partial v^{(k)}}{\partial t} = I_m^{(k)} - \frac{1}{R_m^{(k)}} (v^{(k)} - v_{\text{rest}}), \quad \text{on } \Gamma_i^{(k)}, \quad (12f)$$

$$v^{(k)}|_{t=0} = v_0^{(k)}, \quad \text{on } \Gamma_i^{(k)}, \quad (12g)$$

$$I_m^{(1,2)} = (\sigma_i \nabla u_i^{(2)}) \cdot \hat{\mathbf{n}}_i^{(2)} = -(\sigma_i \nabla u_i^{(1)}) \cdot \hat{\mathbf{n}}_i^{(1)}, \quad \text{on } \Gamma^{(1,2)}, \quad (12h)$$

$$w^{(1,2)} = u_i^{(1)} - u_i^{(2)}, \quad \text{on } \Gamma^{(1,2)}, \quad (12i)$$

$$C_m^{(1,2)} \frac{\partial w^{(1,2)}}{\partial t} = I_m^{(1,2)} - \frac{1}{R_m^{(1,2)}} (w^{(1,2)} - w_{\text{rest}}), \quad \text{on } \Gamma^{(1,2)}, \quad (12j)$$

$$w^{(1,2)}|_{t=0} = w_0, \quad \text{on } \Gamma^{(1,2)}, \quad (12k)$$

with $k = 1, 2$.

We may use the same method as in Section 3.1 to obtain solutions for u_e , $u_i^{(1)}$, and $u_i^{(2)}$ by solving equations (12a) and (12b) in spherical coordinates and assuming radial symmetry to yield

$$u_e = A_1 \int \frac{1}{\xi^2 \sigma_e} d\xi + A_2, \quad (13a)$$

$$u_i^{(1)} = B_1 \int \frac{1}{\xi^2 \sigma_i} d\xi + B_2, \quad (13b)$$

$$u_i^{(2)} = C_1 \int \frac{1}{\xi^2 \sigma_i} d\xi + C_2, \quad (13c)$$

where $A_k, B_k, C_k, k = 1, 2$, are the constants of integration, which are generally arbitrary functions of time. Assuming that the conductivities are equal, i.e.,

$$\sigma_i = \sigma_e, \quad (13d)$$

equation (12d), for $k = 1, 2$, establishes the following condition for A_1, B_1 , and C_1 :

$$B_1 = C_1 = A_1 := A. \quad (13e)$$

Additionally, from equations (12e) and (12i), we have

$$v^{(1)} = B_2 - A_2, \quad (13f)$$

$$v^{(2)} = C_2 - A_2, \quad (13g)$$

and

$$w^{(1,2)} = u_i^{(1)} - u_i^{(2)} = B_2 - C_2. \quad (13h)$$

The transmembrane current for cell k on the membrane $\Gamma_i^{(k)}$ takes the form

$$I_m^{(k)} = (\sigma_i \nabla u_i^{(k)}) \cdot \hat{\mathbf{n}}_i^{(k)} = -\frac{A}{(\rho_1)^2}, \quad (13i)$$

while the transmembrane current in the gap junction is

$$I_m^{(2,1)} = (\sigma_i \nabla u_i^{(2)}) \cdot \hat{\mathbf{n}}_i^{(2)} = -(\sigma_i \nabla u_i^{(1)}) \cdot \hat{\mathbf{n}}_i^{(1)} = 0. \quad (13j)$$

Now assuming that the cells are characterized by the same model, i.e., $R_m^{(1)} = R_m^{(2)}$ and $C_m^{(1)} = C_m^{(2)}$, we can define initial-value problems using equations (12f) and (12g) to solve for potentials $v^{(k)}$, $k = 1, 2$, resulting in

$$v^{(k)} = e^{-\frac{t}{C_m^{(1)} R_m^{(1)}}} \left(v_0^{(k)} + \int_0^t \frac{e^{\frac{\tau}{C_m^{(1)} R_m^{(1)}}}}{C_m^{(1)}} \left(\frac{v_{\text{rest}}}{R_m^{(1)}} - \frac{A}{(\rho_1)^2} \right) d\tau \right). \quad (13k)$$

From eq. (13h), $w^{(1,2)}$ takes the form

$$w^{(2,1)} = (v_0^{(1)} - v_0^{(2)}) e^{-\frac{t}{C_m^{(1)} R_m^{(1)}}}. \quad (13l)$$

We note that the expression above satisfies the initial-value problem created with equations (12j) and (12k) in two cases. The first case is when $v_0^{(2)} = v_0^{(1)}$ and $w_{\text{rest}} = w_0 = 0$; the second case is when $v_0^{(2)} \neq v_0^{(1)}$, $w_0 = 0$, and $C_m^{(1,2)} R_m^{(1,2)} = C_m^{(1)} R_m^{(1)}$. Finally, we are able to determine a solution subject to satisfaction of the boundary condition

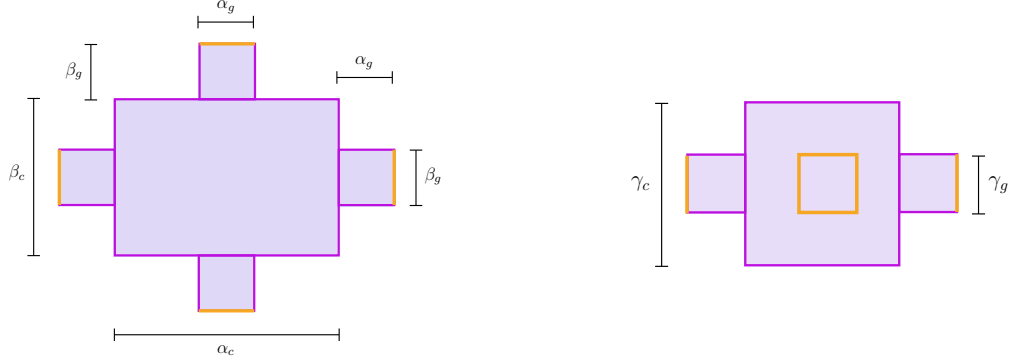
$$u_e|_{\rho=\rho_2} = u_{\text{app}}. \quad (13m)$$

In summary, we have derived a family of solutions under the following conditions: the conductivities σ_i and σ_e are equal, both cells are identical, the resting potential of the gap junction model is zero (which is realistic according to [1]), and the ratio of the membrane capacitance to the gap junction capacitance is equal to the ratio of the cell membrane resistance to the gap junction resistance. Additionally, A and any one of A_2 , B_2 , or C_2 are free to be chosen.

3.3. Manufactured solutions

The method of manufactured solutions (MMS) is a commonly used approach to construct analytical solutions for the differential equations that underlie a simulation code. The key idea behind MMS is to select a smooth and sufficiently differentiable function that satisfies the differential equations and boundary conditions of the problem. The differential equation is then modified by adding forcing (or *source*) terms to ensure that the chosen function becomes a solution of the modified equation. This technique has been used to validate numerical methods for solving the EMI model of a single cell; see, e.g., [1, 4, 3]. In this subsection, we present a manufactured solution for N three-dimensional cells.

Consider a three-dimensional cuboidal extracellular domain with N identical three-dimensional cells embedded in it arranged in a sheet-like structure. The cells are connected with each other through gap junctions; see Figure 4 for a depiction and dimensions of a single cell. To construct a manufactured



(a) xy -plane representation of the single cell.

(b) yz -plane representation of the single cell.

Figure 4: Single three-dimensional cardiac cell and its dimensions: cell membranes (purple) and gap junctions (orange).

solution, we require u_e and $u_i^{(k)}$ to satisfy Poisson's equation, that is,

$$-\nabla \cdot (\sigma_e \nabla u_e) = f_e, \quad (14a)$$

$$-\nabla \cdot (\sigma_i \nabla u_i^{(k)}) = f_i^{(k)}, \quad (14b)$$

with $k = 1, 2, \dots, N$.

Using the method of separation of variables, we propose the following form for the extracellular potential u_e and the intracellular potentials $u_i^{(k)}$:

$$u_e = T_e(t)X(x, y, z), \quad (x, y, z, t) \in \Omega_e \times [t_0, t_f], \quad (14c)$$

$$u_i^{(k)} = T_i^{(k)}(t)X(x, y, z), \quad (x, y, z, t) \in \Omega_i^{(k)} \times [t_0, t_f], \quad (14d)$$

where $T_e = T_e(t)$, $T_i^{(k)} = T_i^{(k)}(t)$, $k = 1, 2, \dots, N$, and $X = X(x, y, z)$ are functions to be determined.

The continuity condition for the normal fluxes in (4b) and (4d) becomes

$$(\sigma_i T_i^{(k)} - \sigma_e T_e) \nabla X \cdot \hat{\mathbf{n}}_i^{(k)} = 0, \quad \text{on } \Gamma_i^{(k)},$$

and

$$\sigma_i(T_i^{(k)} - T_i^{(\ell)})\nabla X \cdot \hat{\mathbf{n}}_i^{(k)} = 0, \quad \text{on } \Gamma^{(k,\ell)}.$$

To ensure the continuity of normal fluxes across cell membranes and gap junctions, we impose the continuity of the normal flux of X at these domains, that is

$$\nabla X \cdot \hat{\mathbf{n}} = 0, \quad \text{on } \Gamma_i^{(k)} \cup \Gamma^{(k,\ell)},$$

where $\hat{\mathbf{n}}$ is the unit normal vector on $\Gamma_i^{(k)} \cup \Gamma^{(k,\ell)}$, which is defined as $\hat{\mathbf{n}} = \hat{\mathbf{n}}_i^{(k)}$ on $\Gamma_i^{(k)}$ and $\hat{\mathbf{n}} = \hat{\mathbf{n}}_i^{(k)}$ on $\Gamma^{(k,\ell)}$. Now if we set the origin of the system at the center of any cell and consider the dimensions $\alpha_g, \beta_g, \gamma_g, \alpha_c, \beta_c,$ and γ_c described in Figure 4, we can choose the following form for the function X :

$$X = \cos\left(\frac{2\pi x}{\alpha_g}\right) \cos\left(\frac{2\pi y}{\beta_g}\right) \cos\left(\frac{2\pi z}{\gamma_g}\right), \quad (14e)$$

where $\alpha_g, \beta_g,$ and γ_g are divisors of $\alpha_c, \beta_c,$ and $\gamma_c,$ respectively.

We see now that this choice implies that $I_m^{(k)} = 0$ on $\Gamma_i^{(k)}$ and that $I_m^{(k,\ell)} = 0$ on $\Gamma^{(k,\ell)}$. Therefore, using the passive cell models (7) and (8), the partial differential equations for the membrane potentials $v^{(k)}$ and the gap junctions $w^{(k,\ell)}$ in (4) take the form

$$C_m^{(k)} \frac{\partial v^{(k)}}{\partial t} + \frac{1}{R_m^{(k)}} (v^{(k)} - v_{\text{rest}}) = g^{(k)}, \quad \text{on } \Gamma_i^{(k)}, \quad (14f)$$

$$C_m^{(k,\ell)} \frac{\partial w^{(k,\ell)}}{\partial t} + \frac{1}{R_m^{(k,\ell)}} (w^{(k,\ell)} - w_{\text{rest}}) = g^{(k,\ell)}, \quad \text{on } \Gamma_i^{(k,\ell)}, \quad (14g)$$

where $g^{(k)}$ and $g^{(k,\ell)}$ are forcing functions to be determined.

We can now choose the form of the time-dependent functions $T_i^{(k)}$ and T_e . Using a similar approach as for X , we select the following simple solutions

$$T_i^{(k)} = A^{(k)} e^{\left(-\frac{t}{C_m^{(k)} R_m^{(k)}}\right)} + T_e, \quad T_e = B, \quad (14h)$$

where $A^{(k)}$, and B are constants that represent the initial values of the functions $T_i^{(k)}$, and T_e .

Using (1) and (2), we can define $g^{(k)}$ and $g^{(k,\ell)}$ as

$$g^{(k)} = -\frac{v_{\text{rest}}}{R_m^{(k)}}, \quad (14i)$$

$$g^{(k,\ell)} = \left(\frac{1}{R_m^{(k,\ell)}} - \frac{C_m^{(k,\ell)}}{C_m^{(k)} R_m^{(k)}} \right) u_i^{(k)} - \left(\frac{1}{R_m^{(k,\ell)}} - \frac{C_m^{(k,\ell)}}{C_m^{(\ell)} R_m^{(\ell)}} \right) u_i^{(\ell)} - \frac{w_{\text{rest}}}{R_m^{(k,\ell)}}, \quad (14j)$$

respectively.

Finally, using (14a) and (14b) the forcing functions f_e and $f_i^{(k)}$ can be taken as

$$f_e = \sigma_e \left(\left(\frac{2\pi}{\alpha_g} \right)^2 + \left(\frac{2\pi}{\beta_g} \right)^2 + \left(\frac{2\pi}{\gamma_g} \right)^2 \right) u_e, \quad (14k)$$

$$f_i^{(k)} = \sigma_i \left(\left(\frac{2\pi}{\alpha_g} \right)^2 + \left(\frac{2\pi}{\beta_g} \right)^2 + \left(\frac{2\pi}{\gamma_g} \right)^2 \right) u_i^{(k)}, \quad (14l)$$

and the boundary condition on $\Gamma_e \times [t_0, t_f]$ can be given by

$$u_{\text{app}} = T_e X, \quad (14m)$$

for Dirichlet boundary condition and

$$I_{\text{app}} = T_e \sigma_e \nabla X \cdot \hat{\mathbf{n}}_e, \quad (14n)$$

for Neumann boundary condition.

4. Numerical solutions

This section describes a numerical method to simulate the presented exact solutions to the EMI model. We employ the mortar finite element method to discretize the spatial domain and operator splitting to discretize the time evolution.

4.1. Spatial discretization using the mortar finite element method

For simplicity, we present the spatial discretization for two cells using Equation (12) subject to Dirichlet boundary conditions. This discretization can easily be extended to N cells or reduced to a single cell. Our presentation follows a similar approach to that in [1].

Multiplying by an appropriate test function ϕ_i and integrating by parts, equations (12a) and (12b) for $k = 1, 2$, can be rewritten in the weak form as

$$\int_{\Omega_i^{(1)}} \sigma_i \nabla u_i^{(1)} \cdot \nabla \phi_i^{(1)} dx + \int_{\Gamma_i^{(1)}} I_m^{(1)} \phi_i^{(1)} ds + \int_{\Gamma^{(2,1)}} I_m^{(1,2)} \phi_i^{(1)} ds = 0 \quad \forall \phi_i^{(1)} \in V_i^{(1)}, \quad (15a)$$

$$\int_{\Omega_i^{(2)}} \sigma_i \nabla u_i^{(2)} \cdot \nabla \phi_i^{(2)} dx + \int_{\Gamma_i^{(2)}} I_m^{(2)} \phi_i^{(2)} ds - \int_{\Gamma^{(2,1)}} I_m^{(1,2)} \phi_i^{(2)} ds = 0 \quad \forall \phi_i^{(2)} \in V_i^{(2)}, \quad (15b)$$

$$\int_{\Omega_e} \sigma_e \nabla u_e \cdot \nabla \phi_e dx - \int_{\Gamma_i^{(1)}} I_m^{(1)} \phi_e ds - \int_{\Gamma_i^{(2)}} I_m^{(2)} \phi_e ds = 0 \quad \forall \phi_e \in V_e, \quad (15c)$$

where V_e and $V_i^{(k)}$ are the function spaces on Ω_e and $\Omega_i^{(k)}$, respectively.

Let G be a function space defined over the cell membranes, specifically $\Gamma = \Gamma_i^{(1)} \cap \Gamma_i^{(2)} \cap \Gamma^{(1,2)}$. Multiplying equation eq. (12f) by the test function $\psi^{(k)}$, associated with the space $\Gamma_i^{(k)}$ for $k = 1, 2$, and equation (12j) by $\psi^{(1,2)}$, associated with the space $\Gamma^{(1,2)}$, and integrating over their respective domains, the equations take the form

$$\int_{\Gamma_i^{(1)}} C_m^{(1)} \frac{\partial v^{(1)}}{\partial t} \psi^{(1)} ds = \int_{\Gamma_i^{(1)}} I_m^{(1)} \psi^{(1)} - \frac{1}{R_m^{(1)}} (v^{(1)} - v_{\text{rest}}) \psi^{(1)} ds \quad \forall \psi \in G, \quad (15d)$$

$$\int_{\Gamma_i^{(2)}} C_m^{(2)} \frac{\partial v^{(2)}}{\partial t} \psi^{(2)} ds = \int_{\Gamma_i^{(2)}} I_m^{(2)} \psi^{(2)} - \frac{1}{R_m^{(2)}} (v^{(2)} - v_{\text{rest}}) \psi^{(2)} ds \quad \forall \psi \in G, \quad (15e)$$

$$\int_{\Gamma^{(1,2)}} C_m^{(1,2)} \frac{\partial w^{(1,2)}}{\partial t} \psi^{(1,2)} ds = \int_{\Gamma^{(1,2)}} I_m^{(1,2)} \psi^{(1,2)} - \frac{1}{R_m^{(1,2)}} (w^{(1,2)} - w_{\text{rest}}) \psi^{(1,2)} ds \quad \forall \psi \in G. \quad (15f)$$

Using the same function space defined above, we require our variational problem to satisfy the equations (12e) and (12i). This is achieved by multiplying each equation by the associated test function γ^j , where j corresponds to the respective space as previously defined, and integrating over the appro-

prate domain. That is,

$$\int_{\Gamma_i^{(1)}} (v^{(1)} - u_i^{(1)} + u_e) \gamma^{(1)} ds = 0 \quad \forall \gamma \in G, \quad (15g)$$

$$\int_{\Gamma_i^{(2)}} (v^{(2)} - u_i^{(2)} + u_e) \gamma^{(2)} ds = 0 \quad \forall \gamma \in G, \quad (15h)$$

$$\int_{\Gamma^{(1,2)}} (w^{(1,2)} - u_i^{(1)} + u_i^{(2)}) \gamma^{(1,2)} ds = 0 \quad \forall \gamma \in G. \quad (15i)$$

To describe the finite element discretization of the well-posed problem formulated using equations (15), we introduce $T_{e,h}$ and $T_{i,h}^k$ as the meshes defined over the domains $\Omega_i^{(k)}$ and Ω_e , respectively. The discrete finite element subspaces $V_{e,h}$, $V_{i,h}^k$, and G_h , with h representing the mesh size parameter, are constructed using continuous piecewise linear Lagrange elements. Each subspace is defined on its respective mesh, and the functions in these spaces are linear polynomials on each element of the mesh. That is,

$$\begin{aligned} V_{e,h} &= \{v \in C(T_{e,h}) : v|_K = P^1(K) \quad \forall K \in T_{e,h}\}, \\ V_{i,h}^k &= \{v \in C(T_{i,h}^k) : v|_K = P^1(K) \quad \forall K \in T_{i,h}^k\}, \\ G_h &= \{g \in C(T_h) : g|_K = P^1(K) \quad \forall K \in T_h\}. \end{aligned}$$

4.2. Time evolution via operator splitting

The main idea behind operator splitting is to improve efficiency by splitting a differential equation into simpler parts, such as its linear and nonlinear parts or its stiff and non-stiff parts. This allows each part to be solved with methods that suit its specific characteristics. For example, consider an initial-value problem (IVP)

$$\frac{d\mathbf{y}}{dt} = \mathbf{f}(t, \mathbf{y}) := \mathbf{f}^{[1]}(t, \mathbf{y}) + \mathbf{f}^{[2]}(t, \mathbf{y}), \quad \mathbf{y}(t_0) = \mathbf{y}_0, \quad (16a)$$

$$\frac{d\mathbf{y}^{[1]}}{dt} = \mathbf{f}^{[1]}(t, \mathbf{y}^{[1]}), \quad \frac{d\mathbf{y}^{[2]}}{dt} = \mathbf{f}^{[2]}(t, \mathbf{y}^{[2]}), \quad (16b)$$

where the right-hand side function $\mathbf{f}(t, \mathbf{y})$ of the original ordinary differential equation (ODE) eq. (16a) is additively split into two parts (or *operators*), $\mathbf{f}^{[1]}(t, \mathbf{y})$ and $\mathbf{f}^{[2]}(t, \mathbf{y})$, which are then used to form two ODEs eq. (16b).

To now illustrate the workings of operator-splitting methods, consider the simplest approach: the Lie–Trotter (or Godunov) method [13, 14]. Applied

to the IVP eq. (16a), this method begins by solving the subproblem defined by the operator $\mathbf{f}^{[1]}$ over a time step Δt , using the initial condition from the original problem. The solution of this first subproblem, $\mathbf{y}^{[1]}$, then serves as the initial condition for the second subproblem defined by $\mathbf{f}^{[2]}$, which is also solved over Δt . The solution of the second subproblem provides the approximate solution for the original problem at the end of the time step.

Operator-splitting methods applied to cardiac simulations typically separate the problem into two parts: the cell model, which may be stiff (e.g., [10, 11]), and the spatial propagation (or remainder of the system). However, is it possible to split the problem more, for example, by separating the gating equations as well (see, e.g., [15]). In this work, we adopt a two-splitting of the EMI model, separating the cell models from the propagation component, following Tveito et al. [1] and Dominguez et al. [16]. Yet, a three-splitting, where the membrane and gap junctions are treated separately, naturally arises in this context and may offer advantages, particularly when evaluating high-order methods [17].

For applying the operator-splitting method to equations (15), we can consider the problem as

$$\frac{\partial \mathbf{A}_{\text{EMI}} \mathbf{y}_{\text{EMI}}}{\partial t} = \mathbf{f}_{\text{EMI}}^{[1]}(\mathbf{y}_{\text{EMI}}) + \mathbf{f}_{\text{EMI}}^{[2]}(\mathbf{y}_{\text{EMI}}), \quad \mathbf{y}_{\text{EMI}}(t_0) = \mathbf{y}_{\text{EMI}_0},$$

where $\mathbf{y}_{\text{EMI}} = (u_e, u_i^{(1)}, u_i^{(2)}, v^{(1)}, v^{(2)}, w^{(1,2)})^T$, \mathbf{A}_{EMI} is a matrix such that $\mathbf{A}_{\text{EMI}} \mathbf{y}_{\text{EMI}} = (0, 0, 0, v^{(1)}, v^{(2)}, w^{(1,2)}, 0, 0, 0)^T$, and $\mathbf{y}_{\text{EMI}_0}$ represents the initial

data for variables in \mathbf{y}_{EMI} . Therefore, $\mathbf{f}_{\text{EMI}}^{[1]}$ and $\mathbf{f}_{\text{EMI}}^{[2]}$ take the form

$$\mathbf{f}_{\text{EMI}}^{[1]}(\mathbf{y}_{\text{EMI}}) = \begin{pmatrix} 0 \\ 0 \\ 0 \\ -\frac{1}{C_m^{(1)} R_m^{(1)}}(v^{(1)} - v_{\text{rest}}) \\ -\frac{1}{C_m^{(2)} R_m^{(2)}}(v^{(2)} - v_{\text{rest}}) \\ -\frac{1}{C_m^{(1,2)} R_m^{(1,2)}}(w^{(1,2)} - w_{\text{rest}}) \\ 0 \\ 0 \\ 0 \end{pmatrix},$$

$$\mathbf{f}_{\text{EMI}}^{[2]}(\mathbf{y}_{\text{EMI}}) = \begin{pmatrix} \int_{\Omega_i^{(1)}} \sigma_i \nabla u_i^{(1)} \cdot \nabla \phi_i^{(1)} dx + \int_{\Gamma_i^{(1)}} I_m^{(1)} \phi_i^{(1)} ds + \int_{\Gamma^{(2,1)}} I_m^{(1,2)} \phi_i^{(1)} ds \\ \int_{\Omega_i^{(2)}} \sigma_i \nabla u_i^{(2)} \cdot \nabla \phi_i^{(2)} dx + \int_{\Gamma_i^{(2)}} I_m^{(2)} \phi_i^{(2)} ds - \int_{\Gamma^{(2,1)}} I_m^{(1,2)} \phi_i^{(2)} ds \\ \int_{\Omega_e} \sigma_e \nabla u_e \cdot \nabla \phi_e dx - \int_{\Gamma_i^{(1)}} I_m^{(1)} \phi_e ds - \int_{\Gamma_i^{(2)}} I_m^{(2)} \phi_e ds \\ \int_{\Gamma_i^{(1)}} \frac{I_m^{(1)}}{C_m^{(1)}} \psi^{(1)} ds \\ \int_{\Gamma_i^{(2)}} \frac{I_m^{(2)}}{C_m^{(2)}} \psi^{(2)} ds \\ \int_{\Gamma^{(1,2)}} \frac{I_m^{(1,2)}}{C_m^{(1,2)}} \psi^{(1,2)} ds \\ \int_{\Gamma_i^{(1)}} (v^{(1)} - u_i^{(1)} + u_e) \gamma^{(1)} ds \\ \int_{\Gamma_i^{(2)}} (v^{(2)} - u_i^{(2)} + u_e) \gamma^{(2)} ds \\ \int_{\Gamma^{(1,2)}} (w^{(1,2)} - u_i^{(1)} + u_i^{(2)}) \gamma^{(1,2)} ds \end{pmatrix}.$$

This methodology was implemented using the `Firedrake` package [18]

for spatial discretization, and the `pythOS` and `irksome` libraries [19, 20] to handle time evolution via operator splitting.

5. Examples of numerical solutions

In this section, we present examples of numerical computations that were performed in order to verify the agreement with and stability of the exact solutions to the EMI model as described in Section 3 using the numerical approach described in Section 4.

5.1. Accuracy

To assess the accuracy of the exact solutions described in section 4.2, we evaluate the L^2 -norm of the error for each variable $v^{(k)}$, $u_i^{(k)}$, $w^{(k,\ell)}$, and u_e in experiments. The L^2 -norm of the error of a quantity y is defined as

$$\|\tilde{y} - y\|_2 = \left(\int_{\Omega} |\tilde{y} - y|^2 dx \right)^{\frac{1}{2}},$$

where \tilde{y} and y denote the numerical and analytical solutions, respectively, and Ω represents the domain of y .

5.2. Experiments

To simulate the examples presented in sections 3.1 and 3.2, it is necessary to exclude the origin to avoid the singularity inherent in the solutions and ensure convergence of the numerical approximation. Accordingly, we exclude a circular or hemisphere region centered at the origin within the respective domains and impose Dirichlet boundary conditions on the resulting boundary for the corresponding variables. The meshes for these domains are generated using `Gmsh` [21].

For simplicity, we set the EMI model parameters as $C_m^{(k)} = C_m^{(k,\ell)} = 1$ for all simulations. For Experiments 1 and 2, the boundary has a radius of 6, while the intracellular space has a radius of 5. Additionally, the origin is excluded by removing a circular or spherical region of radius 3. The conductivities are set to $\sigma_i = \sigma_e = 1$.

5.2.1. *Experiment 1: Sinusoidal pulse*

Choosing the cell model with parameters $R_m^{(1)} = 1$ and $v_{\text{rest}} = 5$, and setting $A = 10 \sin(t)$, $A_2 = 5$ and $v_0 = 20$ in equations (11), the exact solution for a single cell takes the form of a sinusoidal pulse:

$$\begin{aligned} u_e &= 10 \sin(t) \ln(r) + 5, \\ u_i^{(1)} &= \sin(t)(10 \ln(r) - 1) + \cos(t) + 14e^{-t} + 10, \\ v^{(1)} &= 14e^{-t} + \cos(t) - \sin(t) + 5, \end{aligned}$$

with extracellular boundary condition

$$u_{\text{app}} = 10 \ln(6) \sin(t) + 5.$$

Table 1: Errors for Experiment 1. Simulation time spans are from $t_0 = 0.25$ to $t_f = 7$, n_f denotes the number of time steps, and h represents the characteristic length of the mesh.

h	n_f	$\ \tilde{u}_e - u_e\ _2$	$\ \tilde{u}_i^{(1)} - u_i^{(1)}\ _2$	$\ \tilde{v}^{(1)} - v^{(1)}\ _2$
0.40	7	9.035×10^{-1}	3.575	5.929
0.28	14	4.164×10^{-1}	1.651	2.736
0.20	28	2.016×10^{-1}	8.006×10^{-1}	1.326
0.14	56	9.937×10^{-2}	3.947×10^{-1}	6.536×10^{-1}
0.10	112	4.932×10^{-2}	1.960×10^{-1}	3.246×10^{-1}

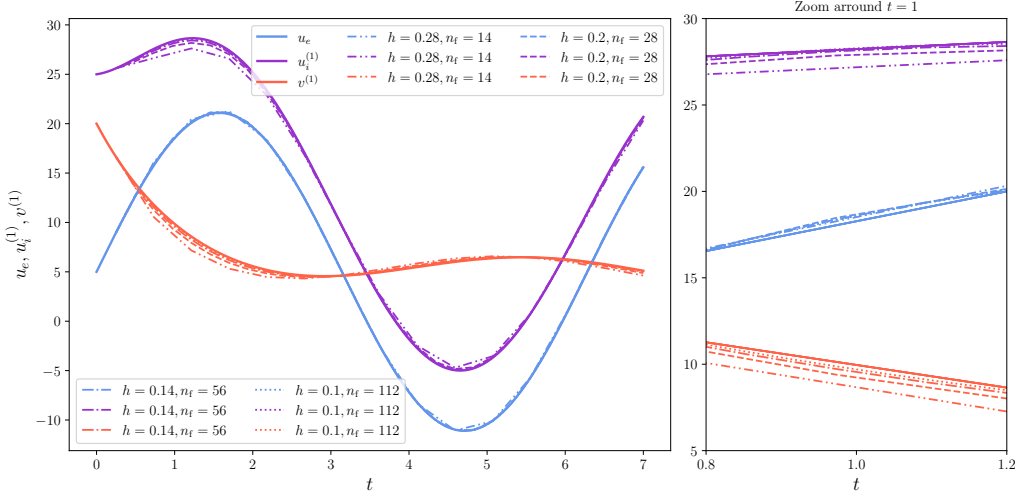


Figure 5: Numerical and exact solutions for u_e , $u_i^{(1)}$, and $v^{(1)}$ at $r = 5$, in Experiment 1.

Table 1 demonstrates the correct implementation of the numerical method for the single-cell model. The table shows that the L^2 -norm of the error for the variables $v^{(1)}$, $u_i^{(1)}$, and u_e decreases as the mesh size and time step decrease. In addition, fig. 5 illustrates that the numerical solutions converge to the exact solutions as the mesh size and time step are refined.

5.2.2. Experiment 2: Damped cosine pulse

Using the same cell model as in section 5.2.1 and setting $A = -50e^{-\frac{t}{10}} \cos(t)$, $A_2 = 0$, $v_0^{(1)} = 10$ and $v_0^{(2)} = 30$ in equations (13), the exact solution for two-coupled spherical cells takes the form of a damped cosine pulse:

$$\begin{aligned}
 u_e &= \frac{50e^{-\frac{t}{10}} \cos(t)}{\rho}, \\
 u_i^{(k)} &= 5 + \frac{e^{-t}(144k + 581)}{181} + \frac{2e^{-\frac{t}{10}} \left((905 + 18\rho) \cos(t) + 20\rho \sin(t) \right)}{181\rho}, \\
 v^{(k)} &= 5 + \frac{e^{-t}(144k + 581)}{181} + \frac{20e^{-\frac{t}{10}} (9 \cos(t) + 10 \sin(t))}{181}, \\
 w^{(1,2)} &= -20e^{-t},
 \end{aligned}$$

with $k = 1, 2$. The extracellular boundary condition is given by

$$u_{\text{app}} = \frac{50e^{-\frac{t}{10}} \cos(t)}{6}.$$

Table 2: Errors for Experiment 2. Simulation time spans are from $t_0 = 0.25$ to $t_f = 7$, n_t denotes the number of time steps, and h represents the characteristic length of the mesh. The calculation domain for variables $u_i^{(1)}$, $u_i^{(2)}$, and $w^{(1,2)}$ is $4 \leq \rho \leq 5$.

h	n_t	$\ \tilde{u}_e - u_e\ _2$	$\ \tilde{u}_i^{(1)} - u_i^{(1)}\ _2$	$\ \tilde{u}_i^{(2)} - u_i^{(2)}\ _2$	$\ \tilde{v}^{(1)} - v^{(1)}\ _2$	$\ \tilde{v}^{(2)} - v^{(2)}\ _2$	$\ \tilde{w}^{(1,2)} - w^{(1,2)}\ _2$
0.40	10	5.107×10^{-1}	3.311	2.987	4.476	4.361	3.921×10^{-1}
0.28	20	1.985×10^{-1}	1.872	1.457	2.237	2.061	3.224×10^{-1}
0.20	40	8.778×10^{-2}	1.129	7.751×10^{-1}	1.211	1.055	2.499×10^{-1}
0.14	80	4.840×10^{-2}	7.161×10^{-1}	4.362×10^{-1}	6.954×10^{-1}	5.672×10^{-1}	1.887×10^{-1}
0.10	160	3.404×10^{-2}	4.701×10^{-1}	2.573×10^{-1}	4.182×10^{-1}	3.174×10^{-1}	1.399×10^{-1}

In figs. 6 and 7, we observe that the numerical solutions converge toward the exact solutions as the mesh size and time step decrease. Furthermore, table 2 confirms the correct implementation of the numerical method. It is worth noting that the domain for the L^2 -norm of the error in the variables $u_i^{(1)}$, $u_i^{(2)}$, and $w^{(1,2)}$ is truncated to exclude points near the boundary. This is because Dirichlet boundary conditions are imposed, meaning that convergence near these points is not guaranteed due to the lack of control over the Neumann behavior.

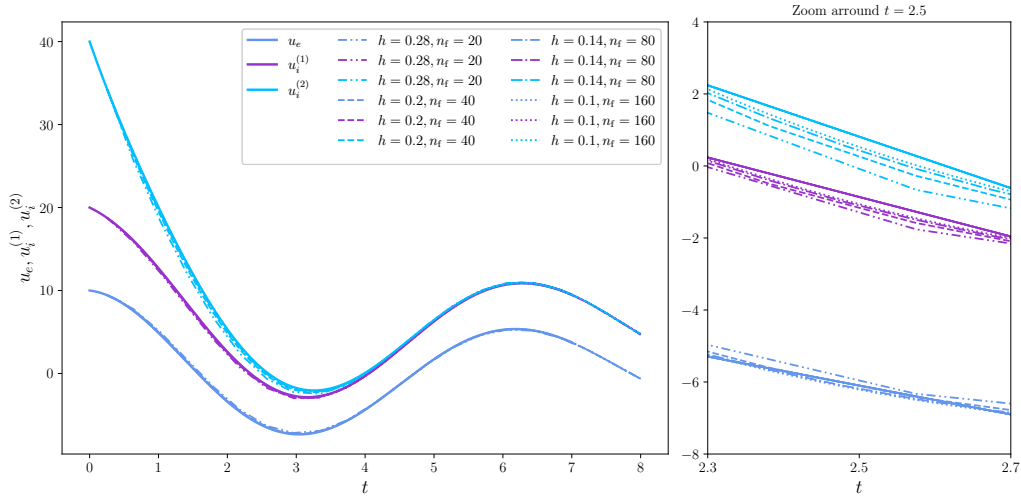


Figure 6: Numerical and exact solutions for u_e , $u_i^{(1)}$, and $u_i^{(2)}$ at $\rho = 5$ in Experiment 2.

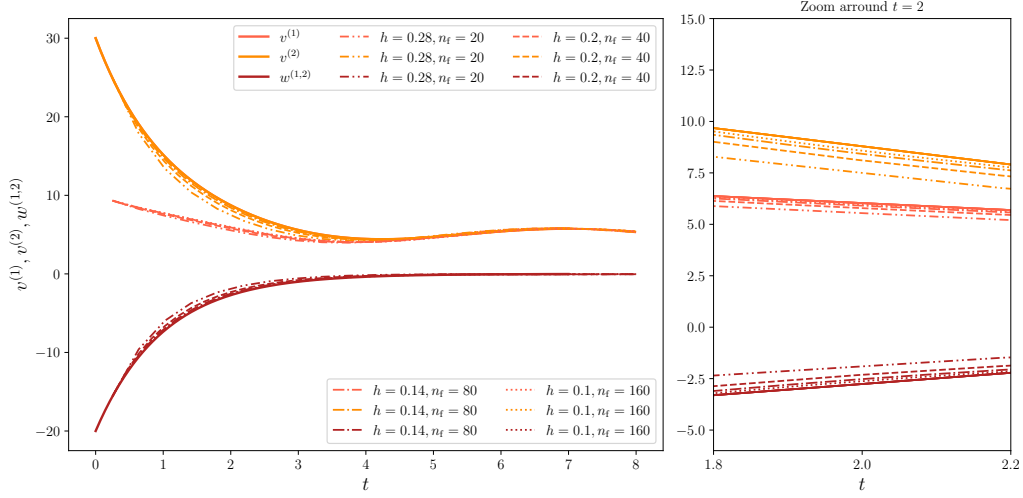


Figure 7: Numerical and exact solutions for $v^{(1)}$ and $v^{(2)}$ at $\rho = 5$, and $w^{(1,2)}$ at $\rho = 4.5$ in Experiment 2.

5.2.3. Experiment 3: 4-cell manufactured solution

For the 4-cell manufactured solution, we consider the passive cell model with parameters $R_m^{(1)} = 1$ and $v_{\text{rest}} = 0$. Additionally, we set the intracellular and extracellular conductivities to $\sigma_i = 1$ and $\sigma_e = 4$. For $T_e = 1$, $T_i^{(k)} = ke^{-t} + T_e$ with cell dimensions $\alpha_g = \beta_g = \gamma_g = 0.5$ and $\alpha_c = \beta_c = \gamma_c = 1$, the exact solution for the 4-cell system is given by

$$\begin{aligned}
 u_e &= \cos(4\pi x) \cos(4\pi y) \cos(4\pi z), \\
 u_i^{(k)} &= (1 + ke^{-t}) \cos(4\pi x) \cos(4\pi y) \cos(4\pi z), \\
 v^{(k)} &= ke^{-t} \cos(4\pi x) \cos(4\pi y) \cos(4\pi z), \\
 w^{(k,\ell)} &= (k - \ell)e^{-t} \cos(4\pi x) \cos(4\pi y) \cos(4\pi z),
 \end{aligned}$$

with forcing terms

$$\begin{aligned}
 f_e &= 192\pi^2 \cos(4\pi x) \cos(4\pi y) \cos(4\pi z), \\
 f_i^{(k)} &= 48(1 + ke^{-t})\pi^2 \cos(4\pi x) \cos(4\pi y) \cos(4\pi z), \\
 g^{(k)} &= g^{(k,\ell)} = 0,
 \end{aligned}$$

for $k, l \in \{1, 2, 3, 4\}$. Enclosing the cells in a cube with dimensions $4.75 \times 4.75 \times 1.75$ to represent the extracellular bound-

ary condition to

$$u_{\text{app}} = 0.$$

Table 3: Errors for intracellular and extracellular potentials in Experiment 3. The simulation time spans are from $t_0 = 0$ to $t_f = 1$, n_f denotes the number of time steps, and h the characteristic length of the mesh.

h	n_f	$\ \tilde{u}_e - u_e\ _2$	$\ \tilde{u}_i^{(1)} - u_i^{(1)}\ _2$	$\ \tilde{u}_i^{(2)} - u_i^{(2)}\ _2$	$\ \tilde{u}_i^{(3)} - u_i^{(3)}\ _2$	$\ \tilde{u}_i^{(4)} - u_i^{(4)}\ _2$
1.4×10^{-1}	10	4.403×10^{-1}	1.342×10^{-1}	3.768×10^{-1}	1.601×10^{-1}	4.337×10^{-1}
1.0×10^{-1}	20	2.902×10^{-1}	8.653×10^{-2}	2.400×10^{-1}	1.053×10^{-1}	2.869×10^{-1}
7.0×10^{-2}	40	1.666×10^{-1}	4.197×10^{-2}	1.158×10^{-1}	5.348×10^{-2}	1.511×10^{-1}
4.9×10^{-2}	80	9.349×10^{-2}	2.368×10^{-2}	6.612×10^{-2}	3.042×10^{-2}	8.897×10^{-2}
3.5×10^{-2}	160	4.982×10^{-2}	1.295×10^{-2}	3.385×10^{-2}	1.660×10^{-2}	2.021×10^{-2}

Table 4: Errors for transmembrane potentials in Experiment 3. The simulation time spans are from $t_0 = 0$ to $t_f = 1$, n_f denotes the number of time steps, and h the characteristic length of the mesh.

h	n_f	$\ \tilde{v}^{(1)} - v^{(1)}\ _2$	$\ \tilde{v}^{(2)} - v^{(2)}\ _2$	$\ \tilde{v}^{(3)} - v^{(3)}\ _2$	$\ \tilde{v}^{(4)} - v^{(4)}\ _2$
1.4×10^{-1}	10	1.973×10^{-1}	5.414×10^{-1}	2.367×10^{-1}	6.351×10^{-1}
1.0×10^{-1}	20	1.353×10^{-1}	3.711×10^{-1}	1.583×10^{-1}	4.414×10^{-1}
7.0×10^{-2}	40	6.336×10^{-2}	1.867×10^{-1}	7.525×10^{-2}	2.408×10^{-1}
4.9×10^{-2}	80	3.623×10^{-2}	1.104×10^{-1}	4.291×10^{-2}	1.400×10^{-1}
3.5×10^{-2}	160	2.021×10^{-2}	6.181×10^{-2}	2.338×10^{-2}	7.824×10^{-2}
h	n_f	$\ \tilde{w}^{(1,2)} - w^{(1,2)}\ _2$	$\ \tilde{w}^{(1,3)} - w^{(1,3)}\ _2$	$\ \tilde{w}^{(2,4)} - w^{(2,4)}\ _2$	$\ \tilde{w}^{(3,4)} - w^{(3,4)}\ _2$
1.4×10^{-1}	10	2.821×10^{-2}	4.395×10^{-2}	5.263×10^{-2}	7.484×10^{-2}
1.0×10^{-1}	20	3.944×10^{-2}	3.376×10^{-2}	4.871×10^{-2}	5.011×10^{-2}
7.0×10^{-2}	40	1.904×10^{-2}	2.596×10^{-2}	2.700×10^{-2}	2.941×10^{-2}
4.9×10^{-2}	80	1.111×10^{-2}	1.375×10^{-2}	1.546×10^{-2}	1.711×10^{-2}
3.5×10^{-2}	160	5.800×10^{-3}	6.865×10^{-3}	8.464×10^{-3}	9.078×10^{-3}

The results presented in Tables 3 and 4 validate the correct implementation of the numerical method and the accuracy of the 4-cell manufactured solution. The L^2 -norm of the errors for the variables u_e , $v^{(k)}$, $u_i^{(k)}$, and $w^{(k,\ell)}$ with $k, \ell \in \{1, 2, 3, 4\}$ consistently decrease as the mesh size and time step are refined.

6. Conclusions

The EMI model provides a powerful framework for modeling cardiac tissue. However, its high computational cost limits its application. This limitation drives the development of new computational methods and hence highlights the utility of analytical solutions for establishing the accuracy and efficiency of software. In this work, we derived a family of analytical solutions for the EMI model for both a single circular cell (eq. (11)) and two coupled semi-spherical cells (eq. (13)), assuming radial symmetry and equal conductivities in the intracellular and extracellular spaces. This last assumption has relevance when modeling liposomes. Although these solutions diverge at the origin, we demonstrate that they can be accurately simulated by excluding the origin from the domain and imposing Dirichlet boundary conditions on the resulting boundary for the corresponding variables. This approach makes the solutions suitable for the convergence analysis of numerical methods. We simulated some simple examples to demonstrate the convergence of numerical solutions to the analytical ones; see, sections 5.2.1 and 5.2.2. Additionally, we present a manufactured solution for N three-dimensional cells (eq. (14)) that was used to simulate 4 cells and validated the accuracy of the numerical implementation; see, section 5.2.3. Altogether, these solution form a benchmark for assessing the accuracy of numerical methods for solving the EMI model. Furthermore, the Python implementation of the numerical method provides a solid foundation for future research on the convergence analysis of high-order operator splitting methods.

Data availability

The dataset supporting this study is available at <https://doi.org/10.5281/zenodo.14948002>. The source code to reproduce the data can be accessed in the following repository: <https://github.com/uofs-simlab/EMI-Analytical-Solutions>.

References

- [1] A. Tveito, K. H. Jæger, M. Kuchta, K.-A. Mardal, M. E. Rognes, A cell-based framework for numerical modeling of electrical conduction in cardiac tissue, *Frontiers in Physics* 5 (2017) 48. doi:10.3389/fphy.2017.00048.

URL <https://www.frontiersin.org/article/10.3389/fphy.2017.00048>

- [2] G. R. de Souza, R. Krause, S. Pezzuto, Boundary integral formulation of the cell-by-cell model of cardiac electrophysiology, *Engineering Analysis with Boundary Elements* 158 (2024) 239–251.
- [3] N. Berre, M. E. Rognes, A. Massing, Cut finite element discretizations of cell-by-cell EMI electrophysiology models, *SIAM Journal on Scientific Computing* 46 (4) (2024) B527–B553.
- [4] A. J. Ellingsrud, M. Kuchta, A splitting, discontinuous Galerkin solver for the cell-by-cell electroneutral Nernst–Planck framework, *arXiv preprint arXiv:2404.08320* (2024).
- [5] D. Fokoué, Y. Bourgault, Numerical analysis of finite element methods for the cardiac extracellular-membrane-intracellular model: Steklov–Poincaré operator and spatial error estimates, *ESAIM: Mathematical Modelling and Numerical Analysis* 57 (4) (2023) 2595–2621.
- [6] M. Veneroni, Reaction-diffusion systems for the microscopic cellular model of the cardiac electric field, *Mathematical methods in the applied sciences* 29 (14) (2006) 1631–1661.
- [7] P. C. Franzone, G. Savaré, Degenerate evolution systems modeling the cardiac electric field at micro-and macroscopic level, in: *Evolution Equations, Semigroups and Functional Analysis: in memory of Brunello Terreni*, Springer, 2002, pp. 49–78.
- [8] F. Henríquez, C. Jerez-Hanckes, F. Altermatt, Boundary integral formulation and semi-implicit scheme coupling for modeling cells under electrical stimulation, *Numerische Mathematik* 136 (1) (2017) 101–145.
- [9] K. H. Jæger, A. Tveito, Derivation of a cell-based mathematical model of excitable cells, *Modeling excitable tissue* (2021) 1–13.
- [10] K. H. W. J. ten Tusscher, A. V. Panfilov, Cell model for efficient simulation of wave propagation in human ventricular tissue under normal and pathological conditions, *Physics in Medicine and Biology* 51 (23) (2006) 6141–6156. doi:10.1088/0031-9155/51/23/014.
URL <https://doi.org/10.1088/0031-9155/51/23/014>

- [11] E. Grandi, F. S. Pasqualini, J. L. Puglisi, D. M. Bers, A novel computational model of the human ventricular action potential and Ca transient, *Biophysical Journal* 96 (3, Supplement 1) (2009) 664a – 665a. doi:<https://doi.org/10.1016/j.bpj.2008.12.3513>.
URL <http://www.sciencedirect.com/science/article/pii/S0006349508037533>
- [12] R. A. Gray, P. Pathmanathan, A parsimonious model of the rabbit action potential elucidates the minimal physiological requirements for alternans and spiral wave breakup, *PLOS Computational Biology* 12 (10) (2016) 1–21. doi:[10.1371/journal.pcbi.1005087](https://doi.org/10.1371/journal.pcbi.1005087).
URL <https://doi.org/10.1371/journal.pcbi.1005087>
- [13] H. F. Trotter, Approximation of semi-groups of operators, *Pacific Journal of Mathematics* 8 (4) (1958) 887–919. doi:[10.2140/pjm.1958.8.887](https://doi.org/10.2140/pjm.1958.8.887).
URL <https://projecteuclid.org/euclid.pjm/1103039709>
- [14] S. Godunov, A difference method for numerical calculation of discontinuous solutions of the equation of hydrodynamics, *Matematicheskii Sbornik* 47 (89-3) (1959) 271–306.
- [15] K. R. Green, R. J. Spiteri, Gating-enhanced IMEX splitting methods for cardiac monodomain simulation, *Numerical Algorithms* 81 (2019) 1443–1457.
- [16] S. Domínguez, J. Reimer, K. R. Green, R. Zolfaghari, R. J. Spiteri, A simulation-based method to study the LQT1 syndrome remotely using the EMI model, *Emerging Technologies in Biomedical Engineering and Sustainable TeleMedicine* (2021) 179–189.
- [17] R. J. Spiteri, A. Tavassoli, S. Wei, A. Smolyakov, Beyond Strang: A practical assessment of some second-order 3-splitting methods, *Communications on Applied Mathematics and Computation* (2023) 1–20.
- [18] D. A. Ham, P. H. J. Kelly, L. Mitchell, C. J. Cotter, R. C. Kirby, K. Sagiya, N. Bouziani, S. Vorderwuelbecke, T. J. Gregory, J. Beteridge, D. R. Shaper, R. W. Nixon-Hill, C. J. Ward, P. E. Farrell, P. D. Brubeck, I. Marsden, T. H. Gibson, M. Homolya, T. Sun, A. T. T. McRae, F. Luporini, A. Gregory, M. Lange, S. W. Funke, F. Rathgeber,

- G.-T. Bercea, G. R. Markall, Firedrake User Manual, Imperial College London and University of Oxford and Baylor University and University of Washington, first edition Edition (5 2023). doi:10.25561/104839.
- [19] V. Guenter, S. Wei, R. J. Spiteri, pythOS: A Python library for solving IVPs by operator splitting, arXiv preprint arXiv:2407.05475 (2024).
- [20] P. E. Farrell, R. C. Kirby, J. Marchena-Menendez, Irksome: Automating Runge–Kutta time-stepping for finite element methods, ACM Transactions on Mathematical Software (TOMS) 47 (4) (2021) 1–26.
- [21] C. Geuzaine, J.-F. Remacle, Gmsh: A 3-D finite element mesh generator with built-in pre- and post-processing facilities, International Journal for Numerical Methods in Engineering 79 (11) (2009) 1309–1331. doi:10.1002/nme.2579.
URL <https://onlinelibrary.wiley.com/doi/abs/10.1002/nme.2579>